

# The ortho-to-para ratio of $\text{H}_2\text{Cl}^+$ : Quasi-classical trajectory calculations and new simulations in light of new observations

R. Le Gal<sup>1</sup>, C. Xie<sup>2</sup>, E. Herbst<sup>1</sup>, D. Talbi<sup>3</sup>, H. Guo<sup>2</sup>, and S. Muller<sup>4</sup>

<sup>1</sup> Departments of Chemistry and Astronomy, University of Virginia, McCormick Road, Charlottesville, VA 22904, USA, e-mail: romane.le\_gal@cfa.harvard.edu\*

<sup>2</sup> Department of Chemistry and Chemical Biology, University of New Mexico, Albuquerque, New Mexico, 87131, USA

<sup>3</sup> Laboratoire Univers et Particules de Montpellier, Université de Montpellier, CNRS, Place Eugène Bataillon, 34095 Montpellier, France

<sup>4</sup> Department of Space, Earth and Environment, Chalmers University of Technology, Onsala Space Observatory, SE-43992 Onsala, Sweden

Received 13 July 2017; Accepted 22 August 2017

## ABSTRACT

Multi-hydrogenated species with proper symmetry properties can present different spin configurations, and thus exist under different spin symmetry forms, labeled as para and ortho for two-hydrogen molecules. We investigated here the ortho-to-para ratio (OPR) of  $\text{H}_2\text{Cl}^+$  in the light of new observations performed in the  $z=0.89$  absorber toward the lensed quasar PKS 1830–211 with the Atacama Large Millimeter/submillimeter Array (ALMA). Two independent lines of sight were observed, to the southwest (SW) and northeast (NE) images of the quasar, with OPR values found to be  $3.15 \pm 0.13$  and  $3.1 \pm 0.5$  in each region, respectively, in agreement with a spin statistical weight of 3:1. An OPR of 3:1 for a molecule containing two identical hydrogen nuclei can refer to either a statistical result or a high-temperature limit depending on the reaction mechanism leading to its formation. It is thus crucial to identify rigorously how OPRs are produced in order to constrain the information that these probes can provide. To understand the production of the  $\text{H}_2\text{Cl}^+$  OPR, we undertook a careful theoretical study of the reaction mechanisms involved with the aid of quasi-classical trajectory calculations on a new global potential energy surface fit to a large number of high-level ab initio data. Our study shows that the major formation reaction for  $\text{H}_2\text{Cl}^+$  produces this ion via a hydrogen abstraction rather than a scrambling mechanism. Such a mechanism leads to a 3:1 OPR, which is not changed by destruction and possible thermalization reactions for  $\text{H}_2\text{Cl}^+$  and is thus likely to be the cause of observed 3:1 OPR ratios, contrary to the normal assumption of scrambling.

**Key words.** astrochemistry – ISM: molecules – quasars: absorption lines – quasars: individual: PKS 1830–211 – galaxies: ISM – radio lines: galaxies

## 1. Introduction

Di-hydrogenated species, with identical hydrogen nuclei, can be found in two different nuclear spin states: ortho, with a total hydrogen nuclear spin  $I = 1$ , and para, with a total hydrogen nuclear spin  $I = 0$ , with a  $2I + 1$  statistical weight for each state. Similar divisions into two or more spin states occur for molecules with three or more identical hydrogen nuclei. During the last decade, nuclear-spin astrochemistry has gained interest owing to the numerous ortho-to-para ratio (OPR) measurements produced especially by new telescopes with unprecedented sensitivities and high spectral resolution, giving access to previously elusive molecular lines. Such recent OPR determinations include those for  $\text{H}_3^+$  (Crabtree et al. 2011a),  $\text{H}_2\text{O}$  (Lis et al. 2013; Flagey et al. 2013),  $\text{NH}_3$  (Persson et al. 2012),  $\text{NH}_2$  (Persson et al. 2016),  $\text{H}_2\text{S}$  (Crockett et al. 2014),  $\text{H}_2\text{O}^+$  (Schilke et al. 2010; Gerin et al. 2013),  $\text{CH}_2\text{CN}$  (Vastel et al. 2015) and  $\text{H}_2\text{Cl}^+$  (Lis et al. 2010; Gerin et al. 2013). In thermal equilibrium, OPRs for species with two identical protons range from their statistical weight limit of 3:1 at high temperatures to infinity or zero as the temperature decreases, depending on the symmetry of the rotational and electronic wave functions. For example, the  $\text{NH}_2$  thermal OPR, as a

function of decreasing temperature, behaves in an opposite sense from that of  $\text{H}_2$ , due to the  $X^2B_1$  symmetry of the ground electronic state of  $\text{NH}_2$ . OPRs are functions of the temperature only in thermal equilibrium. As an example, in an isolated state, spontaneous radiative ortho-para interconversion for  $\text{H}_2$  are known to be extremely slow,  $\approx 10^{13}$  yr (Raich & Good 1964; Pachucki & Komasa 2008), that is, they are much greater than the age of the Universe (Lique et al. 2014), therefore OPRs were commonly believed to reflect a “formation temperature” (Mumma et al. 1987).

Although some of the observed OPRs were found to be consistent with thermal values, others, such as those of water (Lis et al. 2013; Flagey et al. 2013),  $\text{H}_3^+$  (Crabtree et al. 2011a),  $\text{NH}_3$  (Persson et al. 2012), and  $\text{NH}_2$  (Persson et al. 2016) were not. As an example, for the non-thermal observational values of the OPR of the radical  $\text{NH}_2$  measured toward four high-mass star-forming regions and found to lie, depending on the position observed along the lines-of-sight, either below the high temperature limit of three (2.2 – 2.9) or above this limit ( $\sim 3.5$ ,  $\geq 4.2$ , and  $\geq 5.0$ ) (Persson et al. 2016). A careful theoretical study was necessary to explain all the results. Indeed, although the use of nuclear-spin selection rules (Oka 2004), leads to the reproduction of most of the observed OPR values below three at reasonable temperatures (Le Gal et al. 2014a,b), it was necessary to identify a mecha-

\* new affiliation: Harvard-Smithsonian Center for Astrophysics, 60 Garden St., Cambridge, MA 02138, USA

nism able to at least partially thermalize the OPR at the very low temperatures where the thermal OPR exceeds three and goes to infinity as the temperature goes to 0 K. This need led Persson et al. (2016) to consider a process previously omitted in models: the poorly studied  $\text{H} + \text{NH}_2$  H-atom exchange reaction to interconvert  $\text{NH}_2$  between its ortho and para forms, thus increasing the OPR with decreasing temperature. This suggestion was confirmed by Le Gal et al. (2016) who performed quasi-classical trajectory (QCT) calculations to show that the H-exchange reaction  $\text{NH}_2 + \text{H}$  can indeed proceed without a barrier, and therefore be efficient in the temperature range of interest.

An understanding of these values requires a comprehensive analysis of the processes governing the interstellar nuclear-spin chemistry including the formation and destruction reactions and possible conversions of the different spin symmetries both in the gas and solid phases. Indeed, even an understanding of what appear to be thermal values under interstellar conditions can require a detailed analysis. Once well understood, OPRs can afford new powerful astrophysical diagnostics on the chemical and physical conditions of their environments, and in particular can trace their history, provided that the memory of a chemical process can be propagated and preserved in the molecular level population distributions (Oka 2004; Faure et al. 2013; Le Gal et al. 2014a).

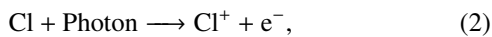
## 2. The case of the Chloronium ion

In this paper we consider the reactions and mechanisms responsible for the observed OPRs of  $\text{H}_2\text{Cl}^+$ . This ion has been detected in a variety of galactic sources, including diffuse and translucent interstellar clouds, the Orion Molecular Cloud, the Orion Bar photodissociation regions (Lis et al. 2010; Neufeld et al. 2012, 2015) and the  $z = 0.89$  absorber toward the lensed quasar PKS 1830–211 (Muller et al. 2014a). The measured OPR values range between 2.5 and 3.2 (although with somehow large uncertainties), roughly consistent with a 3:1 OPR.

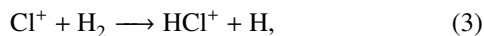
To properly interpret these OPR values, we needed to constrain the main reactions leading to the formation and destruction of  $\text{H}_2\text{Cl}^+$  and possible interconversion of ortho- $\text{H}_2\text{Cl}^+$  and para- $\text{H}_2\text{Cl}^+$ , such as by the H-exchange reaction (Neufeld et al. 2015):



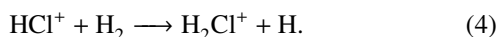
Because Cl can be photoionized to produce  $\text{Cl}^+$  in diffuse gas since its ionization potential ( $12.97 \text{ eV} = 299.1 \text{ kcal/mol}$ ) is just below that of atomic hydrogen:



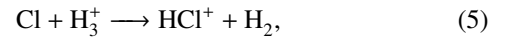
$\text{H}_2\text{Cl}^+$  can be produced as the result of the successive hydrogenations (Neufeld & Wolfire 2009)



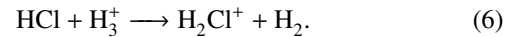
and



To dominate other synthetic pathways, this reactional scheme needs the photoionization of Cl to be efficient, as will occur in diffuse and translucent gas but not in clouds of higher column density where UV radiation is highly attenuated. In such media, proton transfer reaction from  $\text{H}_3^+$  and other protonating ions to Cl and HCl are likely to be competitive; for example,



which competes with reactions (2) and (3), and



which competes with reaction (4) to form the  $\text{H}_2\text{Cl}^+$  OPR. Therefore reactions (4) and (6) can both contribute to the determination of the  $\text{H}_2\text{Cl}^+$  OPR. It should be noted that the  $\text{H}_3^+ + \text{Cl} \longrightarrow \text{H}_2\text{Cl}^+ + \text{H}$  reaction is not considered in the present study. Until recently, with an extra energy needed to dissociate  $\text{H}_3^+$  into  $\text{H}_2^+ + \text{H}$ , such a process was assumed to be non-competitive for reactions of other atoms with  $\text{H}_3^+$  (e.g. Talbi et al. 1991). But recent measurements show that for the reactions  $\text{C} + \text{H}_3^+$  and  $\text{O} + \text{H}_3^+$ , the production of  $\text{CH}_2^+$  and  $\text{H}_2\text{O}^+$  can be competitive (Vissapragada et al. 2016; de Ruelle et al. 2016). More work is clearly needed on the  $\text{Cl} + \text{H}_3^+$  system.

To determine the contributions of reactions (4) and (6) in the  $\text{H}_2\text{Cl}^+$  OPR formation, we must first find out if one reaction dominates the other in rate or whether both are comparable. And secondly, we need to identify whether these reactions occur via a simple hydrogen atom abstraction process for reaction (4) and proton hop process for reaction (6) or via a full scrambling process in which both H-abstraction/proton hop and H-exchange can occur. Taking reaction (4) as an example, the term ‘‘H-exchange’’ refers to a process in which both H atoms on  $\text{H}_2$  end up on  $\text{Cl}^+$  while the original H on  $\text{HCl}^+$  leaves, while ‘‘H-abstraction’’ is a simple process in which an H of  $\text{H}_2$  hops to  $\text{HCl}^+$ . As for reaction (6), the term ‘‘proton hop’’ is used similarly to the term ‘‘H-abstraction’’ when a proton hops from an hydrogenated ion to the molecule with which it reacts to form the new hydrogenated molecular ion in each of its plausible nuclear-spin configurations. Being able to distinguish which mechanism dominates allows one to identify the spin state(s) of the product  $\text{H}_2\text{Cl}^+$  and their expected ratio. For example, a simple hydrogen abstraction in reaction (4) or a simple proton hop in reaction (6) leads to an OPR of 3:1, while scrambling will lead to a different value depending on the OPR of  $\text{H}_2$  for reaction (4) and on the OPR of  $\text{H}_3^+$  for reaction (6). Thus, the resulting formation OPR for  $\text{H}_2\text{Cl}^+$  depends upon whether (i) an intermediate complex can be formed and (ii) its lifetime is long enough to allow the reaction to occur through a scrambling process (Oka 2004; Herbst 2015). Consequently, Oka’s theory (Oka 2004) cannot be used unambiguously without detailed knowledge of the dynamics of a chemical reaction, which requires the study of the potential energy surface (PES) as well as trajectory studies to determine the dominant mechanism leading to the products. In its basic form, Oka’s theory indeed imposes a full proton scrambling for all products involving proton spin distinctions, although it can also be used for restriction to hydrogen abstraction. The approach also contains the assumption that the reaction is sufficiently exothermic so that enough product rotational states can be populated to not constrain calculated ortho-para distributions.

These different mechanisms have been explored to interpret the OPR values of  $\text{H}_3^+$  (Crabtree et al. 2011b,c) and subsequently studied in more detail for the specific system  $\text{H}_2 + \text{H}_3^+$  (Gomez-Carrasco et al. 2012). The mechanistic distinctions were also recently considered for observations of the OPRs of  $\text{H}_2\text{O}^+$  (Herbst 2015) and  $\text{H}_2\text{Cl}^+$  (Neufeld et al. 2015), providing new insights to explore. A rigorous determination of the mechanisms in a particular system requires a full quantum scattering treatment, but as pointed out by Gomez-Carrasco et al. (2012), full quantum computations are rarely achievable because of their complexity and the computational cost. The next best approach is the semi-classical trajectory method, in which atoms and molecules

undergo classical trajectories on a quantum mechanical PES. It is this approach that is used in this paper. Of course, both destruction and conversion processes must also be considered in determining OPRs, and such processes are also contained in our chemical simulations.

In the remainder of the paper, we first consider in Sect. 3 the astronomical observations leading to new OPR measurements for  $\text{H}_2\text{Cl}^+$  in an extragalactic absorber. Then we discuss in Sect. 4 our modeling approach and present its outcomes for the scrambling versus hydrogen abstraction/proton hop mechanisms. Section 5 describes our semi-classical treatment of reaction (4), which models show to be the dominant formation process for  $\text{H}_2\text{Cl}^+$ . Finally, Sect. 6 summarizes our results and draws the main conclusions of the present study.

### 3. Observations

#### 3.1. Description of the observations

The ortho and para forms of  $\text{H}_2\text{Cl}^+$  were observed with the Atacama Large Millimeter/submillimeter Array (ALMA) during Early Science cycle 2, in summer 2014. Two different tunings were observed to cover the  $1_{10-1_01}$  transition of ortho- $\text{H}_2\text{Cl}^+$  (rest frequencies  $\sim 189$  GHz, redshifted to  $\sim 100$  GHz, within ALMA Band 3) and the  $1_{11-0_00}$  transitions of para- $\text{H}_2\text{Cl}^+$  (rest frequencies  $\sim 485$  GHz, redshifted to  $\sim 257$  GHz, within ALMA Band 6), respectively. The array was maintained in a configuration providing a synthesized beam resolution of better than  $0.5''$ , sufficient to resolve the two point-like lensed images of PKS 1830–211, separated by  $1''$ . The bandpass calibration was done on the bright quasar 1924–292, and the gain calibration was solved by regular visits on 1832–2039 during the observations. The correlator was set up with spectral windows of 1.875 GHz, providing a velocity resolution of  $1.3 \text{ km s}^{-1}$  (Band 6) and  $2.9 \text{ km s}^{-1}$  (Band 3), after Hanning smoothing. The data calibration was performed within CASA<sup>1</sup> following a standard procedure. A further run of self-calibration using the bright continuum of PKS 1830–211 helped us to significantly improve the data quality. The final spectra were extracted toward both lensed images of PKS 1830–211, using the CASA-python task UV-MULTIFIT (Martí-Vidal et al. 2014), by fitting a model of two point sources to the interferometric visibilities.

The ALMA spectra of  $\text{H}_2\text{Cl}^+$  toward PKS 1830–211 are shown in Fig. 1. The  $^{37}$ -isotopologues of  $\text{H}_2\text{Cl}^+$  were also detected in the same spectral bands, with a  $^{35}\text{Cl}/^{37}\text{Cl}$  ratio  $\sim 3$ . Since they have weaker absorption, they did not bring a significant improvement on the measurement of the OPR, and they will be reported in another publication.

#### 3.2. Description of the source

The quasar PKS 1830–211 is lensed by a nearly face-on typical spiral galaxy (e.g. Wiklind & Combes 1998; Winn et al. 2002; Koopmans & de Bruyn 2005), and appears as two bright and compact images separated by 1 arcsec, seen at mm wavelengths, and embedded into a pseudo-Einstein ring only seen at cm wavelengths (Jauncey et al. 1991). Molecular absorption arises along the two lines of sight toward the two lensed images, at projected galactocentric radii of  $\sim 2$  kpc for the southwest (SW) image and  $\sim 4$  kpc for the northeast (NE) image, in opposite directions from the center of the absorbing galaxy, respectively. The

absorption system has been observed at mm and submm wavelengths (Muller et al. 2011, 2014b) leading to the detection of more than forty different molecular species toward the SW image. The  $\text{H}_2$  column density is  $\sim 2 \times 10^{22} \text{ cm}^{-2}$  (Muller et al. 2011, 2014b) in this line of sight. In contrast, only about a dozen species have been detected on the NE line of sight, where the  $\text{H}_2$  column density is  $\sim 1 \times 10^{21} \text{ cm}^{-2}$ , that is to say a factor 20 lower.

Molecules tracing gas with a low fraction of molecular hydrogen ( $f_{\text{H}_2}$ ) preferentially, such as  $\text{ArH}^+$ ,  $\text{OH}^+$ ,  $\text{H}_2\text{O}^+$ , and  $\text{H}_2\text{Cl}^+$ , are found to have enhanced abundances along the NE line of sight relative to the SW one (Muller et al. 2014a; Müller et al. 2015; Muller et al. 2016a). Among other evidence, this observation suggests that the absorbing gas in the NE line of sight is more diffuse. The cosmic-ray ionization rate of atomic hydrogen was also investigated using the abundance ratio of  $\text{OH}^+$  and  $\text{H}_2\text{O}^+$  (Muller et al. 2016a), leading to a ratio of about one order of magnitude between the two sightlines.

For the SW absorption, the physical conditions were constrained by Henkel et al. (2008, 2009) using  $\text{NH}_3$  and  $\text{HC}_3\text{N}$  and by Muller et al. (2013) using multi-transition observations of a set of various molecular species ( $\text{CH}_3\text{CN}$ ,  $\text{SO}$ ,  $c\text{-C}_3\text{H}_2$ ,  $\text{HC}_3\text{N}$ ,  $\text{H}^{13}\text{CO}^+$ ,  $\text{H}^{13}\text{CN}$ ,  $\text{HC}^{15}\text{N}$ ,  $\text{HNCO}$ , and  $\text{SiO}$ ). The absorbing gas has properties similar to Galactic diffuse to translucent clouds, with a kinetic temperature of  $\sim 80$  K and an  $\text{H}_2$  volume density of the order of  $10^3 \text{ cm}^{-3}$ . The temperature and density determined by Muller et al. (2013) might be only relevant to the peculiar absorbing component traced by their observed molecules. It is also likely that these conditions are average values over the volume of absorbing gas, which is roughly encompassed in a pencil beam with a base of  $\leq 1$  pc in diameter and a length of few tens to hundreds of pc. See also Schulz et al. (2015) and Muller et al. (2016b) for evidence of inhomogeneities in the absorbing gas.

For the NE line of sight, the conditions are only poorly constrained. There is evidence for a more diffuse gas component than for the SW line of sight. Therefore, the two lines of sight present clearly different physical and chemical gas properties, which makes all the more interesting the comparison of the observed  $\text{H}_2\text{Cl}^+$  OPR between the two.

#### 3.3. Observed absorption spectra

The detection of the para- $\text{H}_2\text{Cl}^+$   $1_{11-0_00}$  line along both the SW and NE lines of sight has already been reported by Muller et al. (2014a). Assuming for each sightline that 3/4 is contributed by the ortho  $\text{H}_2\text{Cl}^+$  and 1/4 by the para  $\text{H}_2\text{Cl}^+$ , they estimated total  $\text{H}_2\text{Cl}^+$  column densities of  $1.4 \times 10^{13} \text{ cm}^{-2}$  in the SW line of sight, and  $4 \times 10^{12} \text{ cm}^{-2}$  in the NE line of sight.

With the new ALMA data reported here of both the ortho- and para- $\text{H}_2\text{Cl}^+$  forms, we can now measure the OPR of  $\text{H}_2\text{Cl}^+$  in the absorber toward PKS 1830–211. We perform a simultaneous fit of the ortho- and para- $\text{H}_2\text{Cl}^+$  absorption profile with five Gaussian velocity components (four for the SW line-of-sight and one for the NE one), with the OPR as a free parameter of the fit. The corresponding fit is shown in Fig. 1. We obtained  $\text{OPR}_{\text{SW}} = 3.15 \pm 0.13$  and  $\text{OPR}_{\text{NE}} = 3.1 \pm 0.5$ , respectively.

### 4. Modeling

The interstellar chemistry of chlorine was first discussed by Jura (1974) and Dalgarno et al. (1974), who identified the most important reactions in the ion-molecule scheme and showed that

<sup>1</sup> <http://casa.nrao.edu/>

**Table 1.**  $\text{H}_2\text{Cl}^+$  lines observed with ALMA.

Species	o/p form	Line	Rest frequency <sup>(a)</sup> (GHz)	Sky frequency <sup>(b)</sup> (GHz)	Dates of observations
$\text{H}_2\text{Cl}^+$	ortho	1 <sub>10</sub> -1 <sub>01</sub>	189.225 <sup>(c)</sup>	100.341	2014, Jul. 21 and Aug. 26
$\text{H}_2\text{Cl}^+$	para	1 <sub>11</sub> -0 <sub>00</sub>	485.418 <sup>(c)</sup>	257.404	2014, Jun. 06 and Jul. 29

**Notes.** *a)* Rest frequencies are taken from the Cologne Database for Molecular Spectroscopy (CDMS, <http://www.astro.uni-koeln.de/cdms/>) and references therein. *b)* Sky frequencies are given assuming a redshift  $z_{abs} = 0.88582$ , heliocentric frame. *c)* The frequency is that of the strongest hyperfine component.

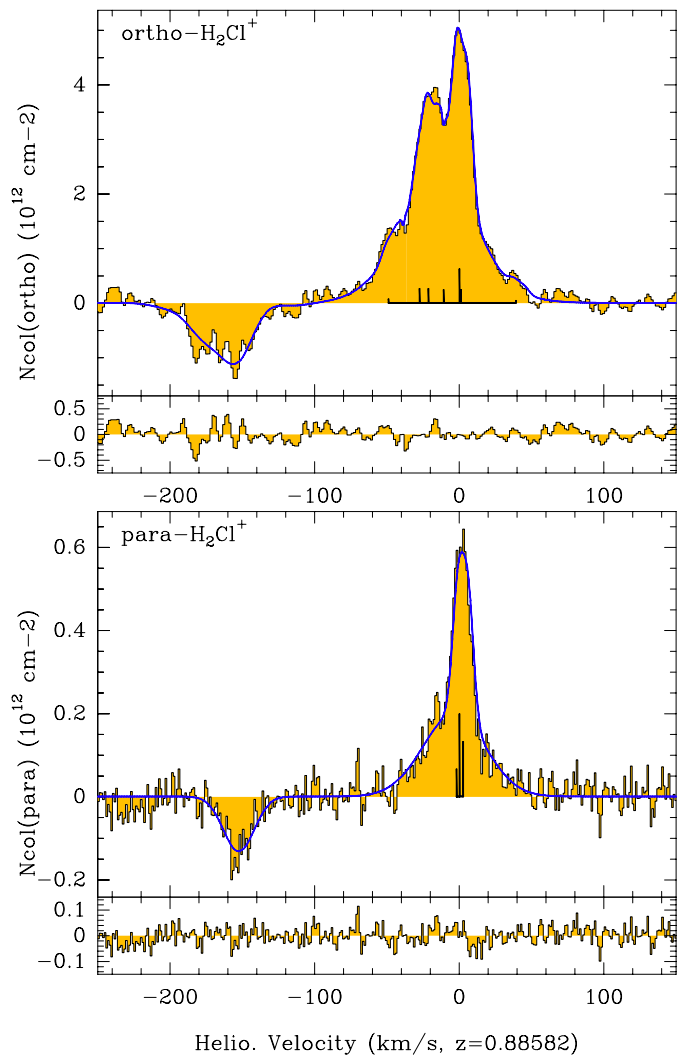


**Fig. 1.** Spectra of the ortho (upper panel) and para (lower panel) forms of  $\text{H}_2\text{Cl}^+$  toward PKS 1830–211. The y-axis is in unit of column density. The opacities were converted into column densities assuming that the excitation is locked to the temperature of the CMB. The spectra of the SW line of sight have been divided by that of the NE. The SW absorption appears as positive feature near  $v = 0 \text{ km s}^{-1}$ , while the NE absorption appears as the negative feature near  $v = -150 \text{ km s}^{-1}$ . The fit with five Gaussian velocity components, including both ortho and para forms, is shown in blue on top of the spectras, and the corresponding residuals are shown in the lower boxes. The velocity scale is set for the strongest hyperfine component. The hyperfine structure is plotted at the base of each spectrum.

$\text{H}_2\text{Cl}^+$  is one of the species produced on the way to HCl. More recently, the study of interstellar chloronium chemistry was re-investigated by Neufeld & Wolfire (2009), who developed a gas-phase chemical network that they coupled with the PDR Meudon Code (Le Petit et al. 2006) to provide, among other chlorine-bearing species,  $\text{H}_2\text{Cl}^+$  abundance predictions for diffuse and translucent clouds. This study and the following study by Neufeld et al. (2012) mainly focused on the total amount of  $\text{H}_2\text{Cl}^+$  and did not consider the different nuclear-spin configurations of  $\text{H}_2\text{Cl}^+$ . In the light of new observations, Neufeld et al. (2015) discussed the different mechanisms that could drive the  $\text{H}_2\text{Cl}^+$  OPR. They focused their discussion on the main formation reaction, reaction (4), and showed how the  $\text{H}_2\text{Cl}^+$  OPR should depend on the OPR of  $\text{H}_2$  if a full scrambling mechanism prevails, while a constant value of 3:1 is obtained with the hydrogen abstraction mechanism. They then showed that the observational data were more consistent with a hydrogen abstraction mechanism, but did not undertake a detailed study of the different plausible mechanisms for reaction (4). Nor did they consider the possibility that reaction (6) can also contribute to the OPR of  $\text{H}_2\text{Cl}^+$ . With our nuclear-spin chemical network – which is the first to our knowledge to consider the different nuclear-spin configurations for  $\text{H}_2\text{Cl}^+$  – and our detailed quantum chemistry and trajectory studies, we have included both of these avenues of research.

#### 4.1. Model description

We enlarged the nuclear spin chemical network used in Le Gal et al. (2016), which includes the hydrogen nuclear-spin chemistry as well as those of other species, with the addition of the chloronium nuclear-spin chemistry that we developed for this work, based on the theory of Oka (2004). Except for the newly added  $\text{H}_2\text{Cl}^+$  spin chemistry, all reactions with distinct spin forms considered in the chemical network proceed via scrambling. For the  $\text{H}_2\text{Cl}^+$  OPR, we included the influence of the different plausible mechanisms, hydrogen abstraction and proton hop versus full scrambling for both reaction (4) and reaction (6), respectively. In addition, we assumed that the destruction reactions for  $\text{H}_2\text{Cl}^+$  are not dependent on its spin state. To run our simulations, we coupled our network to the NAUTILUS code (Ruaud et al. 2016), used in the gas-phase mode, to run pseudo-time-dependent simulations with the use of typical diffuse ISM gas-phase elemental abundances relative to total hydrogen (Gerin et al. 2016), as listed in Table 2. Each pseudo-time-dependent simulation was run with constant physical conditions. The gas was considered shielded from the interstellar radiation field (ISRF Mathis et al. 1983) by one to three magnitudes of visual extinction with a fixed cosmic ray ionization

**Table 2.** Elemental abundances and initial species used in this work.

Species	Elemental abundances <sup>(a)</sup>
He	1.00(-1)
N	6.80(-5)
O	3.10(-4)
H	0.96
$\text{H}_2$	0.02
$\text{C}^+$	1.40(-4)
$\text{S}^+$	1.40(-5)
$\text{Fe}^+$	3.00(-9)
$\text{Cl}^+$	1.80(-7)

**Notes.** Numbers in parentheses are powers of ten. Elemental abundances with respect to the total proton abundance. The electron abundance is computed internally in the code in order to have a neutral gas. <sup>(a)</sup> Elemental abundances from Gerin et al. (2016).

rate of hydrogen that we set equal to the values estimated by Muller et al. (2016a):  $\zeta_{\text{H}_2} \approx 3 \times 10^{-14} \text{ s}^{-1}$  for the SW region and  $\zeta_{\text{H}_2} \approx 5 \times 10^{-15} \text{ s}^{-1}$  for the NE region using the scaling relation  $2.3\zeta_{\text{H}} \approx 1.5\zeta_{\text{H}_2}$  from Glassgold & Langer (1974). The only processes involving dust grains are charge exchanges, dissociative recombinations, and the formation of  $\text{H}_2$ . We adopted a single dust grain radius of  $0.1 \mu\text{m}$ , satisfying a dust-to-gas mass ratio of 1%.

#### 4.2. Modeling results

To test the impact of the physical conditions on  $\text{H}_2\text{Cl}^+$  formation, we ran grids of models where the density,  $n_{\text{H}} = n(\text{H}) + 2n(\text{H}_2)$ , varies from  $2 \times 10^2$  to  $2 \times 10^4 \text{ cm}^{-3}$  and the gas temperature from 10 to 100 K. The results show that the density does not strongly affect the  $\text{H}_2\text{Cl}^+$  OPR but that the temperature does depending on the mechanism considered, as displayed in Fig. 2. The figure represents the  $\text{H}_2\text{Cl}^+$  OPR as function of the temperature for four different models. In addition, the time dependence of the models is designated in the lower panel. The thermal equilibrium value is plotted on the figure, as is the result of our detailed model in which the hydrogen abstraction and proton hop mechanisms are considered for the  $\text{H}_2 + \text{HCl}^+$  and  $\text{H}_3^+ + \text{HCl}$  formation reactions, respectively. We also plot the results of our detailed model in which full scrambling is considered for all formation reactions involving nuclear spin forms. This model is the only one with noticeable time dependence. The derived curve at steady state is almost identical to a much simpler model, designated  $\text{OPR}_0$  in the figure, in which an analytical formula was used to express the OPR of  $\text{H}_2\text{Cl}^+$  in terms of the thermal OPR of  $\text{H}_2$  by including only reaction (4), which occurs via scrambling (Neufeld et al. 2015). The excellent agreement at steady-state between these two latter models shows that the importance of reaction (6) is negligible. For the full scrambling model, a time of  $1.5 \times 10^3 \text{ yr}$  is emphasized in the figure as an indicative reference to show how fast the  $\text{H}_2\text{Cl}^+$  OPR reaches its steady state value. Thus we clearly see that an  $\text{H}_2\text{Cl}^+$  OPR of 3:1, even at a temperature as high as 80 K, is excluded with the consideration of a full scrambling mechanism.

Regarding the full scrambling results it might be legitimate to think that once the OPR of  $\text{H}_2\text{Cl}^+$  is formed, subsequent thermalization processes could occur as the para-to-ortho interconversion of reaction (1), as suggested in Neufeld et al. (2015).

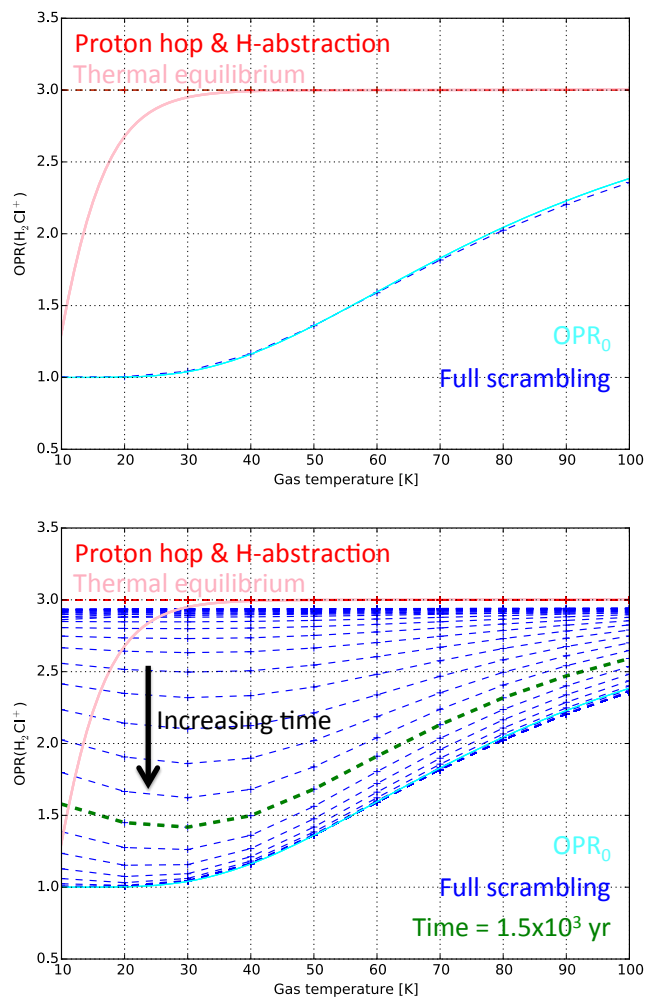


**Fig. 2.**  $\text{H}_2\text{Cl}^+$  OPR as a function of the gas temperature: (i) at thermal equilibrium (solid pink line), (ii) obtained with a full model considering a hydrogen abstraction and a proton hop mechanism for respectively the  $\text{H}_2 + \text{HCl}^+$  and  $\text{H}_3^+ + \text{HCl}$  formation reactions (dashed red curve), (iii) obtained with a model considering full scrambling for all the reactions involving nuclear-spin forms (dashed blue curves), (iv) taken from a simple analytical formula and designated  $\text{OPR}_0$ , this model represents scrambling via reaction (4) at steady state with the OPR for  $\text{H}_2$  treated as thermal (Neufeld et al. 2015) (solid cyan). The time evolution of the complete scrambling model is depicted on the second panel where the  $\text{H}_2\text{Cl}^+$  OPR is represented in green for a time of  $1.5 \times 10^3 \text{ yr}$  as an indicative reference.

Such a mechanism would lead to thermal equilibrium if it could occur rapidly enough. To address this question, we studied the energetics of this reaction in order to investigate whether  $\text{H}_2\text{Cl}^+$  can react with H atoms to interconvert and thermalize the  $\text{H}_2\text{Cl}^+$  OPR, similar to our previous calculation on  $\text{NH}_2 + \text{H}$  (Le Gal et al. 2016) in which  $\text{NH}_2$  is driven toward thermal equilibrium. For the  $\text{H}_2\text{Cl}^+$  case, however, a high barrier was found for this interconversion, as is discussed in Sect. 5. The reaction  $\text{H}_2 + \text{p-}\text{H}_2\text{Cl}^+ \leftrightarrow \text{H}_2 + \text{o-}\text{H}_2\text{Cl}^+$  is even less plausible. If the reaction occurs via H-H exchange, the necessary breaking of  $\text{H}_2$  into two H atoms requires more energy than the  $\text{H} + \text{H}_2\text{Cl}^+$  process, which already possesses a barrier. If the process occurs through the formation of  $\text{H}_4\text{Cl}^+$ , our ab initio calculations show the potential to be repulsive. Therefore the only way to obtain the observed 3:1 OPR for  $\text{H}_2\text{Cl}^+$  seems to be via hydrogen abstraction, and not via scrambling with thermalization afterwards.

Of course, it is possible that there is another and more efficient direction to thermal equilibrium, which we are missing, but it is, in our view, unlikely.

Thus our tentative conclusion is that under diffuse or translucent conditions, the measured OPR values for  $\text{H}_2\text{Cl}^+$  are best explained in terms of a hydrogen abstraction mechanism leading to formation by mainly the reaction (4) followed by no spin dependence in the destruction of this ion and, most critically, no likely rapid interconversion by reaction between the ortho and para forms. But does reaction (4) indeed proceed via hydrogen abstraction? In order to explore more carefully the different mechanism possibilities we determined the PES for the system and ran thousands of QCT to study the dependence on impact parameter and energy for the fraction of trajectories that (i) undergo no reaction, (ii) undergo an H-abstraction, and (iii) undergo an H-exchange. The results are presented in the following section.

## 5. Calculations of the $\text{H}_2 + \text{HCl}^+$ and $\text{H} + \text{H}_2\text{Cl}^+$ reactions

### 5.1. Ab initio calculations

The stationary points on the  $\text{HCl}^+(\text{X}^2\Pi) + \text{H}_2(\text{X}^1\Sigma_g) \rightarrow \text{H}_2\text{Cl}^+(\text{X}^1\text{A}_1) + \text{H}(\text{S})$  and  $\text{H}_2\text{Cl}^+(\text{X}^1\text{A}_1) + \text{H}(\text{S}) \rightarrow \text{H}(\text{S}) + \text{H}_2\text{Cl}^+(\text{X}^1\text{A}_1)$  reaction paths were first searched using the hybrid generalized gradient approximation (GGA) and B3LYP functional (Stephens et al. 1994) in conjunction with the 6-311++G(d,p) Pople-style triple-zeta-valence basis (Dunning 1989; Woon & Dunning 1993; Kendall et al. 1992). This was followed by second-order Moller-Plesset perturbation theory (MP2) with the correlation-consistent polarized valence triple-zeta (cc-pvtz) basis (Gonzalez & Schlegel 1989, 1990). All possible approaches of  $\text{H}_2$  toward  $\text{HCl}^+$  and of  $\text{H}$  toward  $\text{H}_2\text{Cl}^+$  were considered as shown in Fig. 3. The character of each structure was confirmed by a vibrational analysis carried out at the same level making use of analytical second derivative methods. The assignment of the saddle points was performed using an intrinsic reaction coordinate (IRC) calculation. All calculations were carried out by Gaussian 09 software (Frisch et al. 2009). Finally, minima and transition states were recalculated with the explicitly correlated (F12b) version of the unrestricted coupled-cluster method with singles, doubles, and perturbative triples (UCCSD(T)-F12b, Knizia & Werner 2008; Knizia et al. 2009), as implemented in MOLPRO (Werner et al. 2015). The correlation-consistent polarized valence quadruple-zeta basis set with F12 optimized (cc-pVQZ-F12, Peterson et al. 2008) was used.

The resulting lowest energy profiles are shown in Figs 4 and 5, the geometries of the stationary structures are given Tables A.1 and A.2 and the corresponding frequencies in Tables A.3 and A.4. Figure 4 shows that the formation of  $\text{H}_2\text{Cl}^+$  from  $\text{H}_2$  and  $\text{HCl}^+$  involves a barrierless hydrogen abstraction mechanism with the formation of a stable intermediate complex M3. A proton that approaches one of the hydrogens of  $\text{H}_2\text{Cl}^+$  leads to the formation of the M3 complex of Fig. 4. This barrierless approach corresponds to the reverse path of the  $\text{HCl}^+(\text{X}^2\Pi) + \text{H}_2(\text{X}^1\Sigma_g) \rightarrow \text{H}_2\text{Cl}^+(\text{X}^1\text{A}_1) + \text{H}(\text{S})$  reaction (from the products to M3). On the contrary, the approach of the proton toward the chlorine of  $\text{H}_2\text{Cl}^+$  involves a very high energy barrier of 14.547 kcal/mol (7320 K), as can be seen in Fig. 5.

From the two reactions studied only the barrierless  $\text{HCl}^+(\text{X}^2\Pi) + \text{H}_2(\text{X}^1\Sigma_g) \rightarrow \text{H}_2\text{Cl}^+(\text{X}^1\text{A}_1) + \text{H}(\text{S})$  reaction appears to be relevant for the question addressed in this study. To quantify its efficiency, QCT calculations were undertaken.

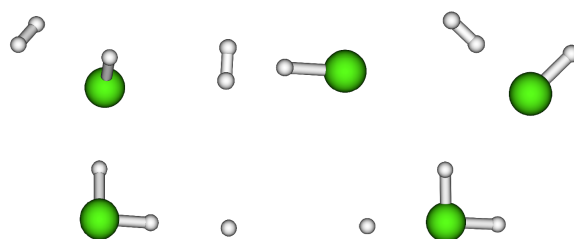


**Fig. 3.** Possible approaches of  $\text{H}_2$  toward  $\text{HCl}^+$  (top) and of  $\text{H}$  toward  $\text{H}_2\text{Cl}^+$  (bottom) considered in this work.

A PES was constructed from the ab initio points spread in all possible configurations accessible by these two reactions. These ab initio points were firstly sampled in the normal mode space of the reactants, products, and stationary points. Additional sets of geometries were then generated by running direct dynamics at the MP2/6-31G(d) level with different initial geometries in the interaction region, using Gaussian 09 (Frisch et al. 2009). These points were recalculated at the same UCCSD(T)-F12b/cc-pVQZ-F12 level cited above. The exothermicity of the reaction  $\text{HCl}^+ + \text{H}_2 \rightarrow \text{H}_2\text{Cl}^+ + \text{H}$  was computed at the UCCSD(T)-F12b level with different basis sets cc-pVTZ-F12 and cc-pVQZ-F12, and the difference is only 0.2%. Based on these points, a primitive PES was first constructed. Classical trajectories with many different initial conditions starting in the reactant, product, and interaction regions were run on the PES to explore the configuration space and improve the PES with new points. These new points were added if they were not too close to the existing points, which was judged by the Euclidean distance ( $< 0.05 \text{ \AA}$ ). This procedure was repeated until convergence was achieved.

### 5.2. PES fitting

A total of 37767 points below 69 kcal/mol relative to the global minimum on the PES were selected and fit using the permutation invariant polynomial-neural network (PIP-NN) method (Jiang & Guo 2013; Li et al. 2013; Jiang et al. 2016). Although no symmetry is considered in the ab initio calculations, the PIP-NN method enforces the invariance of the PES when two identical atoms (H in this case) are exchanged. To enforce the permutation symmetry of the system, symmetry functions in the form of PIPs were used in the input layer of the NN, and the permutation symmetry of all three H atoms was considered. In the PIP-NN approach, the symmetrized polynomials are (Xie & Bowman 2010):

$$G = \hat{S} \prod_{i < j}^N p_{ij}^{l_{ij}}, \quad (7)$$

where  $l_{ij}$  is the order of the monomial,  $\hat{S}$  is the symmetrization operator,  $N$  is the number of atoms, and  $p_{ij} = \exp(-\alpha r_{ij})$  are the Morse-like variables with  $\alpha = 1.0 \text{ \AA}^{-1}$  and the internuclear distances  $r_{ij}$  (Braams & Bowman 2009). All 50 PIPs up to the fourth order were used in the input layer and the NN architecture was selected to be of 20 and 80 neurons for the two hidden layers, resulting in 2781 parameters. The NN fittings were trained using the Levenberg-Marquardt algorithm (Hagan & Menhaj 1994) and the root mean square error (RMSE), defined as:

$$\text{RMSE} = \sqrt{\sum_{i=1}^{N_{\text{data}}} w (E_i^{\text{output}} - E_i^{\text{target}})^2 / N_{\text{data}}}, \quad (8)$$

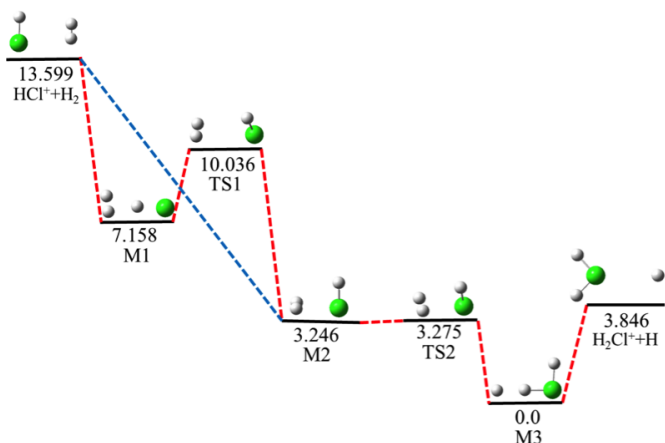


**Fig. 4.** Lowest energy UCCSD(T)-F12/cc-pVQZ-F12 energy profile for the  $\text{HCl}^+(\text{X}^2\Pi) + \text{H}_2(\text{X}^1\Sigma_g) \rightarrow \text{H}_2\text{Cl}^+(\text{X}^1\text{A}_1) + \text{H}(\text{S})$  reaction. The energies of the stationary points are given in kcal/mol relative to the M3 minimum (1 kcal/mol = 503.2 K). Zero point energies are not included.

where  $w$  is the weighing function  $0.1/(0.1 + E)$  with  $E$  relative to the global minimum, and  $E_i^{\text{target}}$  and  $E_i^{\text{output}}$  are the input and fitted energies, respectively. To avoid overfitting, the data were randomly divided into three sets, namely, the training (90% of the data points), validation (5%), and testing (5%) sets. The three best PIP-NN fits have RMSEs for training, validation, testing sets and a maximum deviation of 23.0, 43.8, 80.7 and 10909.9 cal/mol for the first one, 23.0, 57.7, 73.8 and 9766.1 cal/mol for the second one, and 25.3, 48.3, 73.8 and 9932.2 cal/mol for the third one. The RMSE of the averaged PIP-NN PES is 23.0 cal/mol ( $\approx 1.0$  meV  $\approx 11.6$  K), and the maximum deviation is 4 kcal/mol.

The equilibrium geometries and harmonic frequencies of the stationary structures of the reaction profile of Fig. 4 (hereafter designed as ab initio values) are well reproduced by the fitted PES, as shown in Tables A.1 and A.3. Since the molecular system is very floppy near M2 and TS2, as shown in Fig. 4, relatively large differences in the harmonic frequencies of the low-frequency modes exist between the PES and ab initio values at the M2 and TS2 geometries.

### 5.3. QCT calculations

QCT calculations in this work were implemented in VENUS (Hu et al. 1991). The possible violation of the zero-point energy (ZPE) is a major deficiency in the QCT method, especially at low temperatures, since the ZPE then possesses a large fraction of the total energy. Following our previous work (Le Gal et al. 2016) to avoid a violation of the ZPE, the approach proposed by Hase and coworkers (Paul & Hase 2016) was used. Since the  $\text{HCl}^+(\text{X}^2\Pi) + \text{H}_2(\text{X}^1\Sigma_g) \rightarrow \text{H}_2\text{Cl}^+(\text{X}^1\text{A}_1) + \text{H}(\text{S})$  reaction is barrierless and exothermic (9.75 kcal/mol), only the violation of the ZPE in the reactant channel was considered. The calculated reaction energy with the zero-point energy correction is  $\approx 10.25$  kcal/mol, still about 3 kcal/mol smaller than the value based on the JANAF table of  $\approx 13.3$  kcal/mol (Lias et al. 1988). The latter was obtained indirectly and might contain undetermined uncertainties. The CCSD(T) method used here is considered the “gold standard” in computing thermodynamics en-

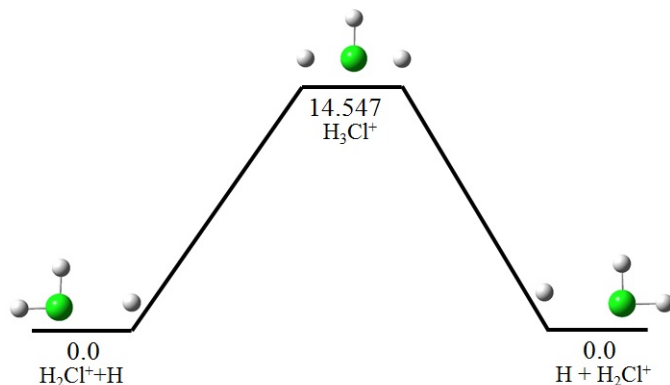


**Fig. 5.** UCCSD(T)-F12/cc-pVQZ-F12 lowest energy profile for the  $\text{H}^+\text{HCl}^+(\text{X}^1\text{A}_1) + \text{H}(\text{S}) \rightarrow \text{H}(\text{S}) + \text{H}^+\text{HCl}^+(\text{X}^1\text{A}_1)$  H-exchange reaction. The energies of the stationary points are given in kcal/mol relative to  $\text{H} + \text{H}_2\text{Cl}^+$ . Zero point energies are not considered.

ergies with an uncertainty that should not exceed a few kcal/mol (Knizia et al. 2009, and references therein) and is thus fairly trustworthy. When a nonreactive trajectory exits the strongly interacting region, the vibrational energies of the  $\text{HCl}^+$  and  $\text{H}_2$  are calculated. If the energy is less than the ZPE, the momenta of all atoms in the system are reversed and the trajectory is forced back to the strongly interacting region without violating energy conservation. Only those trajectories with  $\text{HCl}^+/\text{H}_2$  internal energies larger than the ZPEs are accepted.

The trajectories were initiated with a 15.0 Å separation between reactants, and terminated when products reached a separation of 8.0 Å. The ro-vibrational states of the reactants  $\text{HCl}^+/\text{H}_2$  and relative translational energies were sampled from the Boltzmann distribution at a specific temperature. The propagation time step was chosen as 0.1 fs. Trajectories were discarded if (a) the propagation time reached 30 ps in each interval of two consecutive momentum reversing operations; (b) the number of momentum reversing trajectories exceeds 100; or (c) the total energy failed to converge to 0.05 kcal/mol. The total reaction probability ( $P$ ) for the  $\text{HCl}^+(\text{X}^2\Pi) + \text{H}_2(\text{X}^1\Sigma_g)$  reaction is

$$P = \frac{N_r}{N_{\text{total}}}, \quad (9)$$

where  $N_r$  and  $N_{\text{total}}$  are the number of reactive trajectories and total number of trajectories, respectively. The standard error is given by:

$$\Delta = \sqrt{(N_{\text{total}} - N_r)/N_{\text{total}}N_r}. \quad (10)$$

In the QCT calculations, more than 20000 trajectories were calculated at each temperature, and the statistical errors of the total reaction probabilities are all small. The  $\text{HCl}^+(\text{X}^2\Pi) + \text{H}_2(\text{X}^1\Sigma_g) \rightarrow \text{H}_2\text{Cl}^+(\text{X}^1\text{A}_1) + \text{H}(\text{S})$  reaction has three typical processes, the first is the nonreactive channel, which has three possible outcomes starting from  $\text{HCl}^+ + \text{H}'\text{H}''$ :  $\text{HCl}^+ + \text{H}'\text{H}''$ ,  $\text{H}'\text{Cl}^+ + \text{HH}''$ , and  $\text{H}''\text{Cl}^+ + \text{HH}'$ . It should be noted that the only nonreactive trajectories found in our QCT calculations are those in which no exchange of H atoms take place; i.e.,  $\text{HCl}^+ + \text{H}'\text{H}'' \rightarrow \text{HCl}^+ + \text{H}'\text{H}''$ . The second process is a reactive H-abstraction channel:  $\text{HCl}^+ + \text{H}'\text{H}'' \rightarrow \text{HH}'\text{Cl}^+ + \text{H}''/\text{HH}''\text{Cl}^+ + \text{H}'$ , an example of which is shown in Fig. 6. The last one is a reactive H-exchange channel:  $\text{HCl}^+ + \text{H}'\text{H}'' \rightarrow \text{H}'\text{H}''\text{Cl}^+ + \text{H}$ . The numbers of these three types of trajectories at each temperature

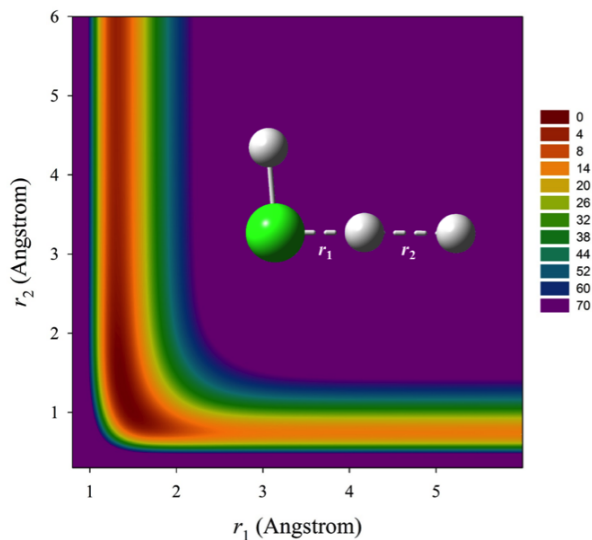


**Fig. 6.** Contour plot for the H-atom abstraction reaction process  $\text{HCl}^+(\text{X}^2\Pi) + \text{H}_2(\text{X}^1\Sigma_g^-) \longrightarrow \text{H}_2\text{Cl}^+(\text{X}^1\text{A}_1) + \text{H}(\text{S})$  reaction along the two reaction coordinates,  $\text{Cl}-\text{H}^{\prime}$  ( $r_1$ ) and  $\text{H}^{\prime}-\text{H}^{\prime\prime}$  ( $r_2$ ) distances, with all the other internal coordinates optimized. The energies are in kcal/mol relative to the global minimum M3.

are listed in Table A.5. It can be readily seen from Table A.5 that the H-abstraction products are dominant for all the studied temperatures ranging from 20 to 300 K. As the temperature decreases, the percentage of the H-exchange trajectories increases. However, at the lowest temperature studied, 20 K, the ratio between the H-exchange and H-abstraction channels is still small (0.85%).

The potential and trajectory studies lead to two principal conclusions: (a) the  $\text{HCl}^+(\text{X}^2\Pi) + \text{H}_2(\text{X}^1\Sigma_g^-)$  reaction proceeds overwhelmingly by an H-abstraction mechanism, which leads to a 3:1 OPR, and (b) the nascent OPR ratio cannot be altered by thermalization reactions involving atomic hydrogen because the process has a large barrier.

## 6. Summary and conclusions

We have presented a detailed study of the nuclear-spin chemistry of  $\text{H}_2\text{Cl}^+$  in which we show that one reaction -  $\text{HCl}^+ + \text{H}_2 \rightarrow \text{H}_2\text{Cl}^+ + \text{H}$  - is mainly responsible for the production of this ion and the OPR obtained during its formation under diffuse or translucent conditions. We then study this reaction in some detail using a QCT method based on the ab initio PES. This research has been undertaken in the light of new ALMA observations of both ortho- and para- $\text{H}_2\text{Cl}^+$  forms in the  $z = 0.89$  absorber toward the quasar PKS 1830–211, along two independent sight lines with different physical properties. In both sightlines, we measured an OPR consistent with a 3:1 ratio. As explained in the present study, for molecules containing two hydrogen atoms and presenting specific symmetry properties, such an OPR is consistent with the spin statistical weight, which can be obtained by high temperatures in which many rotational levels are populated by thermalization processes, or by some mechanism involving reactions that drive the OPR formation, which is subsequently not thermalized. Indeed, two extreme non-thermal reaction mechanisms can be distinguished: (i) a simple hydrogen atom abstraction process or (ii) a full scrambling process in which both H-abstraction and H-exchange can occur, as described in Sect. 2. A

simple H-abstraction can naturally lead to an OPR of 3:1, as is the case here, while scrambling will lead to different values depending upon the OPR of  $\text{H}_2$ , known to trace the thermal history of its environment. In other words, the resulting so-called “formation OPR”, in which destruction and thermalization are not yet considered, depends upon whether the reaction mechanism has a potential well so that (i) an intermediate complex can be formed and (ii) its lifetime is long enough to allow the reactions to occur through a scrambling process (Oka 2004; Herbst 2015).

As a consequence, the theory of Oka (2004), which is used as standard, in which scrambling of H atoms via a long-lived complex is most frequently assumed, should be used with care. It should not be used unambiguously without detailed knowledge of the dynamics of a chemical reaction, which requires the study of the PES as well as trajectory studies to determine the dominant mechanism or mechanisms leading to products. The theory of Oka (2004) also requires exothermic reactions where many product rotational states are populated. If this is not the case, a 3:1 value is unlikely to be achieved. For example if only rotational levels with quantum numbers  $J = 0$  (para) and  $J=1$  (ortho) can be produced, there are nine times as many ortho states as para states. These different types of mechanisms have been explored to interpret the synthesis of the OPR of  $\text{H}_3^+$  (Crabtree et al. 2011b,c) and subsequently studied in more detail for the specific system  $\text{H}_2 + \text{H}_3^+$  (Gomez-Carrasco et al. 2012). More recently, this distinction of mechanisms has been revived in order to explain the observed OPRs of  $\text{H}_2\text{O}^+$  (Herbst 2015) and  $\text{H}_2\text{Cl}^+$  (Neufeld et al. 2015).

Our present study involves the use of QCT calculations on a highly accurate global PES. In this study we show that despite a potential minimum, the mechanism of the reaction between  $\text{H}_2$  and  $\text{HCl}^+$  goes overwhelmingly by a simple H-abstraction angular momentum considerations to a 3:1 OPR. This is consistent with all observations of the chloronium ion including the new observations discussed here. However, one must also consider how the OPR is affected by destruction and thermalization reactions. Although destruction processes are unlikely to affect the OPR of  $\text{H}_2\text{Cl}^+$ , thermalization by reactions with reactive species might be possible, even though such a process with atomic hydrogen has been shown to have a high barrier in the present study (Section 5) and are even less plausible with molecular hydrogen as discussed in Sect. 4.2. For other molecules, given enough time, thermalization might lead to a thermal value of OPR which could reflect the various other temperatures in the sources, as found for instance for the  $\text{NH}_2$  case (Le Gal et al. 2016). From these examples, one must be more careful in assuming that scrambling always takes place when potential minima leading to reaction complexes are present. Although trajectory calculations for reactions involving large numbers of atoms can prove tedious, one can learn a considerable amount from a calculation of the minimum energy pathway.

*Acknowledgements.* The authors thank the anonymous referee for nice and interesting comments. RL is very grateful to Valentine Wakelam for allowing her to use Nautilus in independent research. The authors also warmly thank John Black and Evelyne Roueff for very interesting comments which helped to improve the present manuscript. EH wishes to thank the National Science Foundation for continuing to support the astrochemistry program at the University of Virginia. This paper makes use of the following ALMA data: #2013.1.00020.S. ALMA is a partnership of ESO (representing its member states), NSF (USA) and NINS (Japan), together with NRC (Canada) and NSC and ASIAA (Taiwan) and KASI (Republic of Korea), in cooperation with the Republic of Chile. The Joint ALMA Observatory is operated by ESO, AUI/NRAO and NAOJ. CX and HG are supported by US Department of Energy (Grant No. DE-SC0015997). The computations were performed at the Center for Advanced Research Computing (CARC) at UNM. CX thanks Jun Li for many useful discussions on PIP-NN method. DT acknowledges the HPC resources from GENCI-[CCRT/CINES/IDRIS] (grants



2016 and 2017 [x2016085116-A0020805116] for computing time as well as the Programme National “Physique et Chimie du Milieu Interstellaire” (PCMI) of CNRS/INSU with INC/INP co-funded by CEA and CNES for its support.

## References

- Braams, B. J. & Bowman, J. M. 2009, *Int. Rev. Phys. Chem.*, 28, 577
- Crabtree, K. N., Indriolo, N., Kreckel, H., Tom, B. A., & McCall, B. J. 2011a, *ApJ*, 729, 15
- Crabtree, K. N., Tom, B. A., & McCall, B. J. 2011b, *J. Chem. Phys.*, 134, 194310
- Crabtree, K. N., Kauffman, C. A., Tom, B. A., et al. 2011c, *J. Chem. Phys.*, 134, 194311
- Crockett, N. R., Bergin, E. A., Neill, J. L., et al. 2014, *ApJ*, 781, 114
- Dalgarno, A., de Jong, T., Oppenheimer, M., & Black, J. H. 1974, *ApJ*, 192, L37
- de Ruette, N., Miller, K. A., O'Connor, A. P., et al. 2016, *ApJ*, 816, 31
- Dunning, T. H. 1989, *J. Chem. Phys.*, 90, 1007
- Faure, A., Hily-Blant, P., Le Gal, R., Rist, C., & Pineau des Forêts, G. 2013, *ApJ*, 770, L2
- Flagey, N., Goldsmith, P. F., Lis, D. C., et al. 2013, *ApJ*, 762, 11
- Frisch, M. J., Trucks, G. W., Schlegel, H. B., et al. 2009, *Gaussian 09*, Revision B.01, Gaussian, Inc., Wallingford CT
- Gerin, M., de Luca, M., Lis, D. C., et al. 2013, *J. Phys. Chem. A*, 117, 10018
- Gerin, M., Neufeld, D. A., & Goicoechea, J. R. 2016, *Annu. Rev. Astron. Astrophys.*, 54, 181
- Glassgold, A. E. & Langer, W. D. 1974, *ApJ*, 193, 73
- Gomez-Carrasco, S., González-Sánchez, L., Aguado, A., et al. 2012, *J. Chem. Phys.*, 137, 094303
- Gonzalez, C. & Schlegel, H. B. 1989, *J. Chem. Phys.*, 90, 2154
- Gonzalez, C. & Schlegel, H. B. 1990, *J. Phys. Chem.*, 94, 5523
- Hagan, M. T. & Menhaj, M. B. 1994, *IEEE Transactions on Neural Networks*, 5, 989
- Henkel, C., Braatz, J. A., Menten, K. M., & Ott, J. 2008, *A&A*, 485, 451
- Henkel, C., Menten, K. M., Murphy, M. T., et al. 2009, *A&A*, 500, 725
- Herbst, E. 2015, *EPJ Web of Conferences*, 84, 06002
- Hu, X., Hase, W. L., & Pirraglia, T. 1991, *J. Comput. Chem.*, 12, 1014
- Jauncey, D. L., Reynolds, J. E., Tzioumis, A. K., et al. 1991, *Nature*, 352, 132
- Jiang, B. & Guo, H. 2013, *J. Chem. Phys.*, 139, 054112
- Jiang, B., Li, J., & Guo, H. 2016, *Int. Rev. Phys. Chem.*, 35, 479
- Jura, M. 1974, *ApJ*, 190, L33
- Kendall, R. A., Jr., T. H. D., & Harrison, R. J. 1992, *J. Chem. Phys.*, 96, 6796
- Knizia, G., Adler, T. B., & Werner, H.-J. 2009, *J. Chem. Phys.*, 130, 054104
- Knizia, G. & Werner, H.-J. 2008, *J. Chem. Phys.*, 128, 154103
- Koopmans, L. V. E. & de Bruyn, A. G. 2005, *MNRAS*, 360, L6
- Le Gal, R., Herbst, E., Xie, C., Li, A., & Guo, H. 2016, *A&A*, 596, A35
- Le Gal, R., Hily-Blant, P., Faure, A., et al. 2014a, *A&A*, 562, A83
- Le Gal, R., Hily-Blant, P., & Faure, A. 2014b, in *SF2A-2014: Proceedings of the Annual meeting of the French Society of Astronomy and Astrophysics*, ed. J. Ballet, F. Martins, F. Bournaud, R. Monier, & C. Reylé, 397–401
- Le Petit, F., Nehmé, C., Le Bourlot, J., & Roueff, E. 2006, *Ap. J. Suppl.*, 164, 506
- Li, J., Jiang, B., & Guo, H. 2013, *J. Chem. Phys.*, 139, 204103
- Lias, S. G., Bartmess, J. E., Liebman, J. F., et al. 1988, *J. Phys. Chem. Ref. Data*, Suppl. 1, 17
- Lique, F., Honvault, P., & Faure, A. 2014, *ArXiv e-prints [arXiv:1402.5292]*
- Lis, D. C., Bergin, E. A., Schilke, P., & van Dishoeck, E. F. 2013, *J. Phys. Chem. A*, 117, 9661
- Lis, D. C., Pearson, J. C., Neufeld, D. A., et al. 2010, *A&A*, 521, L9
- Martí-Vidal, I., Vlemmings, W. H. T., Müller, S., & Casey, S. 2014, *A&A*, 563, A136
- Mathis, J. S., Mezger, P. G., & Panagia, N. 1983, *A&A*, 128, 212
- Müller, H. S. P., Müller, S., Schilke, P., et al. 2015, *A&A*, 582, L4
- Müller, S., Beelen, A., Black, J. H., et al. 2013, *A&A*, 551, A109
- Müller, S., Beelen, A., Guélin, M., et al. 2011, *A&A*, 535, A103
- Müller, S., Black, J. H., Guélin, M., et al. 2014a, *A&A*, 566, L6
- Müller, S., Combes, F., Guélin, M., et al. 2014b, *A&A*, 566, A112
- Müller, S., Müller, H. S. P., Black, J. H., et al. 2016a, *A&A*, 595, A128
- Müller, S., Kawaguchi, K., Black, J. H., & Amano, T. 2016b, *A&A*, 589, L5
- Mumma, M. J., Weaver, H. A., & Larson, H. P. 1987, *A&A*, 187, 419
- Neufeld, D. A., Black, J. H., Gerin, M., et al. 2015, *ApJ*, 807, 54
- Neufeld, D. A., Roueff, E., Snell, R. L., et al. 2012, *ApJ*, 748, 37
- Neufeld, D. A. & Wolfire, M. G. 2009, *ApJ*, 706, 1594
- Oka, T. 2004, *J. Mol. Spec.*, 228, 635
- Pachucki, K. & Komasa, J. 2008, *Phys. Rev. A*, 77, 030501
- Paul, A. K. & Hase, W. L. 2016, *J. Phys. Chem. A*, 120, 372
- Persson, C. M., De Luca, M., Mookerjee, B., et al. 2012, *A&A*, 543, A145
- Persson, C. M., Olofsson, A. O. H., Le Gal, R., et al. 2016, *A&A*, 586, A128
- Peterson, K. A., Adler, T. B., & Werner, H.-J. 2008, *J. Chem. Phys.*, 128, 084102
- Raich, J. C. & Good, Jr., R. H. 1964, *ApJ*, 139, 1004
- Ruud, M., Wakelam, V., & Hersant, F. 2016, *MNRAS*, 459, 3756
- Schilke, P., Comito, C., Müller, H. S. P., et al. 2010, *A&A*, 521, L11
- Schulz, A., Henkel, C., Menten, K. M., et al. 2015, *A&A*, 574, A108
- Stephens, P., Devlin, F., Chabalowski, C., & Frisch, M. J. 1994, *J. Phys. Chem.*, 98, 11623
- Talbi, D., Defrees, D. J., Egolf, D. A., & Herbst, E. 1991, *ApJ*, 374, 390
- Vastel, C., Yamamoto, S., Lefloch, B., & Bachiller, R. 2015, *A&A*, 582, L3
- Vissapragada, S., Buzard, C. F., Miller, K. A., et al. 2016, *ApJ*, 832, 31
- Werner, H.-J., Knowles, P. J., Knizia, G., et al. 2015, *MOLPRO*, version 2015.1, a package of ab initio programs, see <http://www.molpro.net>
- Wiklund, T. & Combes, F. 1998, *ApJ*, 500, 129
- Winn, J. N., Kochanek, C. S., McLeod, B. A., et al. 2002, *ApJ*, 575, 103
- Woon, D. E. & Dunning, T. H. 1993, *J. Chem. Phys.*, 98, 1358
- Xie, Z. & Bowman, J. M. 2010, *J. Chem. Theo. Comput.*, 6, 26, pMID: 26614316

## **Appendix A: QCT calculation data**

**Table A.1.** Geometries (lengths in Å and angles in °) of the stationary points for the HCl<sup>+</sup>(X<sup>2</sup>Π) + H<sub>2</sub>(X<sup>1</sup>Σ<sub>g</sub>) → H<sub>2</sub>Cl<sup>+</sup>(X<sup>1</sup>A<sub>1</sub>) + H<sup>(2</sup>S) reaction. “Ab initio” refers to the UCCSD(T)-F12/ cc-pVQZ-F12 optimized values while “PES” refers to the fitted values.

Species	Level	$R_{HH'}$	$R_{HH''}$	$R_{H''Cl}$	$\Theta_{HH'Cl}$	$\Theta_{H''ClH'}$	$\Phi_{HH'ClH''}$
H <sub>2</sub> + HCl <sup>+</sup>	ab initio	0.74148		1.31596			
	PES	0.74151		1.31585			
TS1	ab initio	0.75063	2.06285	1.31670	82.48	41.22	81.34
	PES	0.75046	2.05911	1.31666	82.45	41.26	81.31
M2	ab initio	0.79532	2.39800	1.30530	79.03	87.34	89.36
	PES	0.79498	2.39768	1.30559	78.95	87.25	89.46
TS2	ab initio	0.80189	2.48691	1.30501	99.13	88.31	84.33
	PES	0.80166	2.48873	1.30524	99.04	88.61	83.59
M3	ab initio	1.38323	3.13620	1.30247	179.24	94.35	180.00
	PES	1.38748	3.14005	1.30261	179.22	94.38	180.00
H + H <sub>2</sub> Cl <sup>+</sup>	ab initio			1.30554		94.38	
	PES			1.30542		94.38	

**Table A.2.** Geometries (lengths in Å and angles in °) of the stationary structures for the H<sup>(1</sup>H<sup>)</sup>Cl<sup>+</sup>(X<sup>1</sup>A<sub>1</sub>) + H<sup>(2</sup>S) → H<sup>(2</sup>S) + H<sup>(1</sup>H<sup>)</sup>Cl<sup>+</sup>(X<sup>1</sup>A<sub>1</sub>) reaction. “Ab initio” refers to the the UCCSD(T)-F12/ cc-pVQZ-F12 optimized values.

Species	Level	$R_{H'Cl}$	$R_{H''Cl}$	$R_{HCl}$	$\Theta_{H'ClH''}$	$\Theta_{H''ClH}$	$\Phi_{H'H''ClH}$
H + H <sub>2</sub> Cl <sup>+</sup>	ab initio	1.30554	1.30554			94.38	
TS3	ab initio	1.50695	1.29902	1.50705	89.02	89.02	180.00

**Table A.3.** Relative energies (kcal/mol) and harmonic frequencies (cm<sup>-1</sup>) of the stationary structures for the HCl<sup>+</sup>(X<sup>2</sup>Π) + H<sub>2</sub>(X<sup>1</sup>Σ<sub>g</sub>) → H<sub>2</sub>Cl<sup>+</sup>(X<sup>1</sup>A<sub>1</sub>) + H<sup>(2</sup>S) reaction. “Ab initio” refers to the UCCSD(T)-F12/ cc-pVQZ-F12 optimized values while “PES” refers to the fitted values.

Species	Level	Energy	Frequency					
			1	2	3	4	5	6
H <sub>2</sub> + HCl <sup>+</sup>	ab initio	13.617	4403.8	2681.5				
	PES	13.599	4400.6	2679.7				
TS1	ab initio	9.976	356.5i	4254.9	2662.0	534.1	351.1	211.4
	PES	10.036	361.3i	4238.7	2655.5	538.6	348.5	195.8
M2	ab initio	3.272	3624.0	2757.0	675.8	588.1	385.5	234.6
	PES	3.246	3614.4	2753.2	686.1	596.6	390.9	183.0
TS2	ab initio	3.294	391.7i	3467.2	2744.9	662.5	497.9	199.6
	PES	3.275	256.3i	3481.3	2755.7	702.0	624.3	369.1
M3	ab initio	0.000	2779.6	1974.2	1196.8	545.6	401.8	325.6
	PES	0.000	2780.9	1987.9	1200.2	543.7	404.0	339.8
H + H <sub>2</sub> Cl <sup>+</sup>	ab initio	3.852	2761.5	2752.0	1219.3			
	PES	3.846	2764.3	2751.9	1217.5			

**Table A.4.** Relative energies (kcal/mol) and harmonic frequencies ( $\text{cm}^{-1}$ ) of the stationary structures for the  $\text{H}_2\text{Cl}^+(\text{X}^1\text{A}_1) + \text{H}(\text{S}) \longrightarrow \text{H}(\text{S}) + \text{H}_2\text{Cl}^+(\text{X}^1\text{A}_1)$  reaction. “Ab initio” refers to the UCCSD(T)-F12/cc-pVQZ-F12 optimized values.

Species	Level	Energy	Frequency					
			1	2	3	4	5	6
H + $\text{H}_2\text{Cl}^+$	ab initio	0.0	2761.5	2752.0	1219.3			
TS3	ab initio	14.547	1084.9i	2792.8	1634.0	1219.2	902.6	558.62

**Table A.5.** Numbers of nonreactive and reactive trajectories, maximal impact parameter ( $b_{max}$ ), and total reaction probability ( $P$ ) for the  $\text{HCl}^+(\text{X}^2\Pi) + \text{H}_2(\text{X}^1\Sigma_g^-) \longrightarrow \text{H}_2\text{Cl}^+(\text{X}^1\text{A}_1) + \text{H}(\text{S})$  reaction in the QCT calculations.  $N_{nonreactive}$ ,  $N_{H-abs}$ ,  $N_{H-ex}$ , and  $N_{total}$  denote the numbers of the nonreactive, reactive H-abstraction, reactive H-exchange, and total trajectories, respectively.

$T$ (K)	$b_{max}$ ( $\text{\AA}$ )	$N_{nonreactive}$	$N_{H-abs}$	$N_{H-ex}$	$N_{total}$	$P$
300	11.2	16665	4077	10	20752	$0.197 \pm 0.003$
250	11.4	16719	4405	7	21131	$0.209 \pm 0.003$
200	11.7	16544	4709	10	21263	$0.222 \pm 0.003$
150	12.0	16266	4932	18	21216	$0.233 \pm 0.003$
100	12.5	15791	5509	27	21327	$0.260 \pm 0.003$
50	13.1	16201	6571	42	22814	$0.290 \pm 0.003$
20	13.8	13960	7409	63	21432	$0.349 \pm 0.003$